arXiv:2611.32905v1 [hep-ph] 24 Nov 2026

TeV Gamma-Ray Transparency Bounds on Neutrinos and Axions

Shengyi Liu,[2,*] Hyeonseok Seong,[3,4,2,5,†] Chen Sun,[1,6,7,‡] and Seokhoon Yun[8,9,§]

[1] *School of Fundamental Physics and Mathematical Sciences, Hangzhou Institute for Advanced Study, UCAS, Hangzhou 310024, China*
[2] *Department of Physics and Jockey Club Institute for Advanced Study, The Hong Kong University of Science and Technology, Hong Kong S.A.R., China*
[3] *State Key Laboratory of Dark Matter Physics, Tsung-Dao Lee Institute, Shanghai Jiao Tong University, Shanghai 200240, China*
[4] *Key Laboratory for Particle Astrophysics and Cosmology (MOE) & Shanghai Key Laboratory for Particle Physics and Cosmology, Shanghai Jiao Tong University, Shanghai 200240, China*
[5] *Deutsches Elektronen-Synchrotron DESY, Notkestr. 85, 22607 Hamburg, Germany*
[6] *International Centre for Theoretical Physics Asia-Pacific, Beijing / Hangzhou, China*
[7] *Abdus Salam International Centre for Theoretical Physics, Strada Costiera 11, 34151, Trieste, Italy*
[8] *Department of Physics, Kyungpook National University, Daegu 41566, Korea*
[9] *Particle Theory and Cosmology Group, Center for Theoretical Physics of the Universe, Institute for Basic Science, Daejeon 34126, Korea*

(Dated: November 25, 2026)

Multi-TeV gamma rays propagating over cosmological distances measure the extragalactic background light (EBL) through attenuation by electron–positron pair production. This is particularly valuable in the infrared, where the EBL is difficult to measure directly. Since the growing sample of observed multi-TeV photons provides tight constraints on the EBL photon intensity, this, in turn, constrains new particles that radiatively decay into meV–eV photons. We set the first TeV-transparency bounds on active-neutrino electromagnetic transition moments, obtain new constraints on radiatively decaying sterile neutrinos, and derive competitive limits on the axion–photon coupling.

INTRODUCTION

The extragalactic background light (EBL) is the accumulated optical and infrared radiation produced over the history of galaxies. Unlike the cosmic microwave background, its main contribution is purely astrophysical. Predicting it requires a synthesis of stellar emission, dust reprocessing, galaxy evolution, and the cosmic star-formation history [1]. Consequently, the photon density relevant for the propagation of very-high-energy gamma rays is difficult to compute.

Observationally, the EBL can be determined in three complementary ways. Summed light from resolved galaxies provides a lower bound [2], subject to the completeness of the galaxy catalog. Direct photometry measures the total intensity, but only after bright foregrounds have been subtracted [3]. Finally, attenuation of multi-TeV gamma rays measures the EBL along cosmological lines of sight. Joint fits can reconstruct the EBL spectrum together with the intrinsic blazar spectra [4], an approach also explored for LHAASO blazar observations [5]. A recent analysis of more than 260 archival TeV spectra reconstructed the EBL from 0.18 to 120 μm and found no significant diffuse excess above integrated galaxy light [6]. This agreement makes it possible to constrain new physics that generates an additional cosmological photon population, which is the focus of this Letter.

Throughout, $E_{\rm UV}$ denotes the gamma-ray energy observed today, while $E_{\rm IR}$ denotes the EBL photon's local energy at the interaction redshift z. The gamma ray's local energy is therefore $(1+z)E_{\rm UV}$. The Breit–Wheeler process $\gamma_{\rm UV}\gamma_{\rm IR} \to e^+e^-$ is allowed when

$$2(1+z)E_{\rm UV}E_{\rm IR}(1-\cos\theta) \geq 4m_e^2, \tag{1}$$

where θ is the collision angle. The pair-production cross section and threshold kinematics therefore makes photons above $\mathcal{O}(10)$ TeV especially sensitive to the part of the EBL above 0.01 eV. For a source at redshift z_s, let $\Phi_{\rm int}(E_{\rm UV})$ be the flux that would reach us without EBL absorption. The observed flux is then $\Phi_{\rm obs}(E_{\rm UV}) = \Phi_{\rm int}(E_{\rm UV})e^{-\tau(E_{\rm UV},z_s)}$. An observed multi-TeV spectrum therefore constrains the optical depth and hence a cross-section-weighted photon column density. The intrinsic source spectrum remains a nuisance quantity and is treated explicitly below.

GRB 221009A provides a particularly instructive example. At redshift $z = 0.151$, LHAASO detected more than 140 photons above 3 TeV and emission extending beyond 10 TeV [7]. Such photons traverse a region in which the predicted optical depth varies substantially among EBL prescriptions [8]. Accordingly, how anomalous the event appears is inseparable from the assumed

* sliufp@connect.ust.hk
† hseong0627@gmail.com
‡ chen.sun@ucas.ac.cn
§ seokhoon.yun@knu.ac.kr

EBL model and from the inferred intrinsic burst spectrum. Photon–axion conversion has been tested with blazar spectra under different EBL assumptions [9] and with the LHAASO spectrum of this burst [10]. We therefore do not use GRB 221009A as motivation for a mechanism that evades standard attenuation. Instead, we take its observed high-energy spectrum as the latest empirical update of the EBL: the survival of the photons limits the number density of infrared targets that can be present along the line of sight.

This perspective turns TeV transparency into a probe of particles that inject soft photons into the Universe [11]. Radiative decays such as neutrino dipole transitions ($\nu_i \to \nu_j\gamma$), sterile neutrinos ($\nu_s \to \nu\gamma$), and axions ($a \to \gamma\gamma$) [11] generate diffuse radiation in precisely the energy range selected by multi-TeV gamma rays. Since this contribution is non-negative, it can only increase the pair-production optical depth. The observed transparency thus places an upper bound on the additional photon density δn and, in turn, on the relevant decay rates and couplings. For axions, infrared-background anisotropies have been used to constrain the decay contribution [12], and additional gamma-ray absorption from the resulting EBL photons has been considered in LHAASO sensitivity forecasts [13].

In this Letter we combine the EBL reconstruction based on STeVECat [6, 14] with the LHAASO spectrum of GRB 221009A [7] to obtain the strongest constraint to date on the EBL photon density in the energy range relevant for multi-TeV attenuation. Interpreting any remaining EBL intensity as a possible new-physics photon contribution, δn, we set the first TeV-transparency bounds on active-neutrino electromagnetic transition moments surpassing CMB constraint, obtain new constraints on radiatively decaying sterile neutrinos, and derive the competitive limit on the axion–photon coupling on par with some of the strongest constraints in certain mass window.

ATTENUATION OF TEV PHOTONS

In this and subsequent sections, we use natural units with $\hbar = c = k_{\rm B} = 1$. The quantity measured by gamma-ray attenuation is the pair-production optical depth, rather than an unweighted photon column density. For a gamma ray observed with energy $E_{\rm UV}$ from a source at redshift z_s, propagation through an isotropic photon background gives

$$\tau_\gamma(E_{\rm UV}, z_s) = \int_0^{z_s} dz\, \frac{1}{(1+z)H(z)} \int_{-1}^{1} d\mu\, \frac{1-\mu}{2} \times \int_{E_{\rm IR}^{\rm th}}^{\infty} dE_{\rm IR}\, \frac{dn_\gamma}{dE_{\rm IR}}(E_{\rm IR}, z)\sigma_{\gamma\gamma}(s), \quad (2)$$

where $\mu \equiv \cos\theta$, with θ the angle between the two photon momenta, $s = 2E_{\rm UV}(1+z)E_{\rm IR}(1-\mu)$, and $E_{\rm IR}^{\rm th} = 2m_e^2/[E_{\rm UV}(1+z)(1-\mu)]$. Here $E_{\rm IR}$ is the local EBL photon energy, and $dn_\gamma/dE_{\rm IR}$ is the proper spectral number density, both evaluated at redshift z. The Breit–Wheeler cross section [15] vanishes below threshold and peaks not far above it, making the attenuation energy range moderately broad around $E_{\rm IR}$. Explicitly,

$$\sigma_{\gamma\gamma}(s) = \frac{3\sigma_{\rm T}}{16}(1-\beta_s^2)\left[(3-\beta_s^4)\ln\left(\frac{1+\beta_s}{1-\beta_s}\right) - 2\beta_s(2-\beta_s^2)\right], \quad (3)$$

for $s \geq 4m_e^2$, where $\beta_s = \sqrt{1-4m_e^2/s}$ and $\sigma_{\rm T}$ is the Thomson cross section; below threshold, $\sigma_{\gamma\gamma} = 0$.

In the analysis, we use the EBL reconstructed from more than 260 archival TeV spectra [6]. We also take into account the LHAASO observation of GRB 221009A [7], which extends the sensitivity to the EBL at the infrared energy. To constrain the photon density injected by new physics, we decompose the photon field as

$$\frac{dn_\gamma}{dE_{\rm IR}} = \frac{dn_\gamma^{\rm gal}}{dE_{\rm IR}} + \frac{dn_\gamma^{\rm NP}}{dE_{\rm IR}}, \quad (4)$$

Here n_γ is the total proper EBL photon number density, $n_\gamma^{\rm gal}$ is the standard astrophysical component generated by stellar emission and dust reprocessing over the cosmic star-formation history, and $n_\gamma^{\rm NP}$ is an additional diffuse component produced by new physics. Since Eq. (2) is linear in the target photon density, the same decomposition applies to the optical depth, $\tau_\gamma = \tau_\gamma^{\rm gal} + \tau_\gamma^{\rm NP}$.

Integrated light from resolved galaxies provides a measured floor for $n_\gamma^{\rm gal}$, while the new-physics contribution must be non-negative. We conservatively assign all EBL intensity allowed above that floor to $n_\gamma^{\rm NP}$ and require the resulting optical depth to remain compatible with the gamma-ray data. Any unresolved astrophysical emission occupies part of the same residual and would therefore strengthen the bounds derived below. Figure 1 illustrates this constraint on a diffuse photon population generated by new physics.

INTRINSIC GAMMA-RAY SPECTRA OF EXTRAGALACTIC SOURCES

Extracting the EBL optical depth requires separating propagation from the emission of the source:

$$\Phi_{\rm obs}(E, z) = e^{-\tau_\gamma(E,z)}\Phi_{\rm int}(E), \quad (5)$$

where the intrinsic spectrum $\Phi_{\rm int}(E)$ can be parametrized as [6], for example,

$$\Phi_{\rm int}(E) = \Phi_0 \exp\left[\eta - \Gamma \ln\frac{E}{E_0} - \beta \ln^2\frac{E}{E_0} - \lambda E\right]. \quad (6)$$

The intrinsic spectrum is a flexible phenomenological description of a smooth source continuum. It combines a

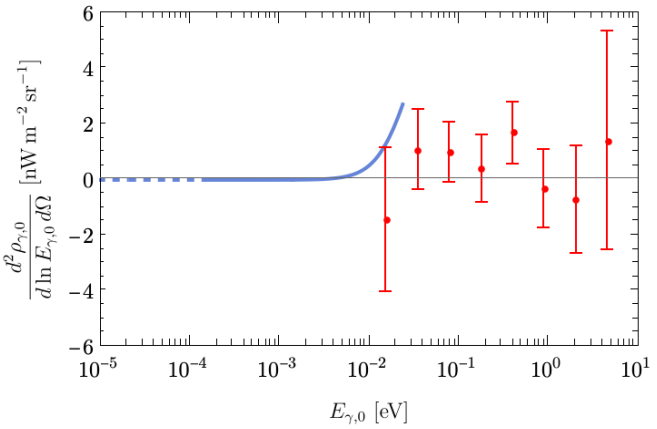


FIG. 1. Present-day residual EBL (red), obtained by subtracting galaxy-count IGL from the gamma-ray reconstruction [2, 6]. Blue: active-neutrino decay with $m_{\rm i} = 0.051\,\text{eV}$, $m_{\rm f} = 0.013\,\text{eV}$, and $\mu_{\rm eff} = 10^{-9}\mu_{\rm B}$. Contributions exceeding the allowed residual predict excessive TeV attenuation.

log-parabolic spectrum with an exponential cutoff. Here E_0 is a fixed pivot energy and Φ_0 is the corresponding reference flux, while the logarithmic normalization η, index Γ, curvature β, and inverse cutoff λ (with $\lambda = E_{\rm cut}^{-1}$ for an ordinary cutoff) are fitted separately for every observation, to account for the intrinsic variation of the spectra. The EBL reconstruction marginalizes over these source parameters rather than fixing an intrinsic spectrum.

The source shape is anchored with gamma-ray data below the strongly absorbed band. The STeVECat analysis combines 268 VHE spectra of 45 sources, measured mainly by H.E.S.S., MAGIC, and VERITAS, with contemporaneous Fermi-LAT spectra whenever available. For 64 observations, the 0.1–100 GeV LAT spectrum—where EBL attenuation is negligible for the redshifts considered— provides a correlated prior on (Γ, β). Its normalization is left free because blazars vary, sometimes on timescales shorter than an observing window; LAT therefore anchors the shape, not the TeV flux level. Spectra without contemporaneous LAT coverage are assigned weakly informative shape priors and are marginalized in the same way.

Intrinsic curvature and EBL attenuation are thus not assumed to be exactly orthogonal: a source cutoff can mimic some additional softening. The converse degeneracy relevant to an upper limit on τ_γ is much weaker. Hiding a large optical depth would require the emitted spectrum to compensate the factor $e^{-\tau_\gamma}$ through an exponential hardening, $\Phi_{\rm int} \propto e^{+\tau_\gamma}$, at the highest energies. Such an upturn is not expected from standard particle-acceleration and radiative-loss physics. In addition, the EBL imprint is shared by many sources and scales with redshift, whereas the intrinsic parameters vary independently. The external low-energy anchor and the joint source sample therefore leave only a limited degeneracy between intrinsic shape and optical depth.

CONSTRAINTS ON NEW PHYSICS

We now translate the allowed non-astrophysical component of the EBL, $n_\gamma^{\rm NP}$, into limits on radiative decays. Consider a homogeneous population of nonrelativistic particles X, each of which emits N_γ photons with rest-frame energy E_* and radiative width Γ_X. If the decay photons propagate freely, cosmological redshifting broadens the monochromatic emission into the present-day spectrum. Evaluating $E_{\rm IR}$ and the photon density at $z = 0$ gives

$$\frac{dn_\gamma}{dE_{\rm IR}}(E_{\rm IR}, 0) = \frac{N_\gamma \Gamma_X n_{X,c}(z_*)}{E_{\rm IR} H(z_*)} \Theta(E_* - E_{\rm IR}), \qquad (7)$$

where z_* is the decay redshift selected by $1 + z_* = E_*/E_{\rm IR}$, and $n_{X,c}$ is the comoving parent abundance, including any depletion. The corresponding intensity is $\nu I_\nu = E_{\rm IR}^2 [dn_\gamma/dE_{\rm IR}](E_{\rm IR}, 0)/(4\pi)$ in natural units. Eq. (7) displays the transparent-propagation limit and is useful for understanding the spectral shape. In obtaining the limits below, we retain the redshift dependence and depletion of the parent population, add the resulting photon density to the target field in Eq. (2), and constrain the extra opacity in $\tau_\gamma^{\rm NP}$. We quote separate 95% exclusions based on the broad-band EBL reconstruction of Gréaux et al. [6] and on the LHAASO spectrum of GRB 221009A [7].

Active neutrino dipole moments

For the radiative transition $\nu_i \to \nu_j \gamma$ through $\mathcal{L} \supset \frac{1}{2}\bar{\nu}^j \sigma_{\mu\nu}(\mu_{ij} + \epsilon_{ij}\gamma_5)\nu^i F^{\mu\nu} + \text{h.c.}$, where i, j are the labels for the mass eigenstates, we define $\mu_{\rm eff}^2 = |\mu_{ij}|^2 + |\epsilon_{ij}|^2$. μ_{ij} and ϵ_{ij} are the magnetic and electric transition moments in the mass basis, and note that this operator flips chirality between the left- and right-handed states. The emitted photon energy and decay width are

$$E_* = \frac{m_i^2 - m_j^2}{2m_i}, \qquad \Gamma_{i\to j} = \frac{\mu_{\rm eff}^2}{8\pi}\left(\frac{m_i^2 - m_j^2}{m_i}\right)^3. \qquad (8)$$

For the standard relic abundance, Fig. 2 shows our TeV-transparency limit on $\mu_{\rm eff}$. For transitions among the three active mass eigenstates, the atmospheric splitting implies $E_* \le \sqrt{|\Delta m_{31}^2|}/2 \simeq 0.025\,\text{eV}$; the curves at larger E_* therefore apply only to a more general neutrino spectrum. For the normal-ordering $\nu_3 \to \nu_2$ transition shown here, the conservative Planck+BAO bound $\sum_i m_i < 0.12\,\text{eV}$ in flat ΛCDM corresponds approximately to $m_{\rm lightest} \lesssim 0.03\,\text{eV}$ [16]. In this mass range, the lower edge of our conditional residual-EBL exclusion

band lies below the COBE/FIRAS spectral-distortion bound [17, 18]. While reactor and solar-neutrino scattering and stellar cooling provide stronger constraints [19–26] (see also [27] for a comprehensive review and [28] for a proposed cosmological probe using line-intensity mapping), we note that these measurements probe different effective combinations of dipole moments, whereas radiative decay selects a particular mass-eigenstate transition [29]. Therefore, these probes are complementary.

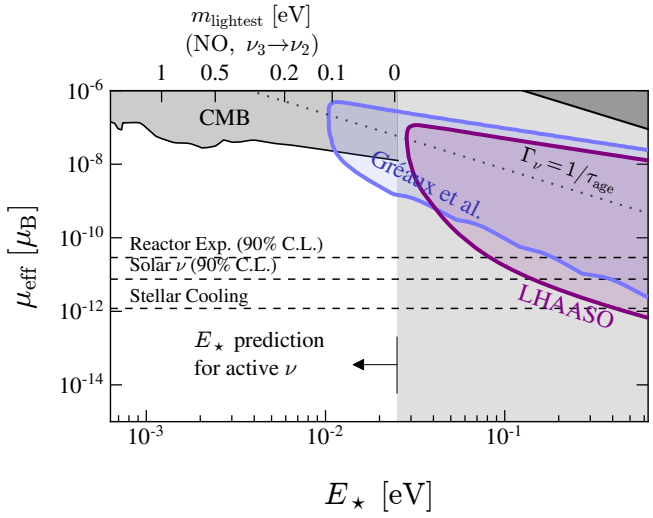


FIG. 2. 95% confidence exclusions for the effective neutrino transition moment versus rest-frame energy E_*. The top axis gives the lightest mass for normal ordering and $\nu_3 \to \nu_2$. Purple: LHAASO [7]; blue: Gréaux et al. [6]. Known active neutrinos require $E_* \leq 0.025\,\text{eV}$; larger energies represent a generic spectrum. Dashed lines: GEMMA [19, 20], solar neutrinos [21, 22], and stellar cooling [23–26]. Gray: CMB [17, 18].

Sterile-neutrino decay

For $\nu_s \to \nu\gamma$, the rest-frame photon energy is

$$E_* = \frac{m_{\nu_s}^2 - m_\nu^2}{2m_{\nu_s}} = \Delta m \left(1 - \frac{\Delta m}{2m_{\nu_s}}\right), \quad \Delta m = m_{\nu_s} - m_\nu. \tag{9}$$

We present the result directly in terms of the radiative width $\Gamma_{\rm sterile}$ for initial sterile-neutrino fractions $f_{\rm sterile} \equiv \rho_{\rm sterile}/\rho_{\rm DM} = 10^{-2}, 10^{-4}, 10^{-6}$ at recombination. A notable feature of this channel is its sensitivity to a highly subdominant population: even when sterile neutrinos constitute far below one percent of the dark matter, their decay photons accumulate over cosmological time and can produce measurable TeV attenuation. The usual structure-formation limits are simultaneously relaxed in this regime. The small-scale power suppression probed by the Lyman-α forest decreases with the warm fraction [30], while the Tremaine–Gunn phase-space mass floor scales approximately as $f_{\rm sterile}^{1/4}$ when the sterile component supplies only a fraction of the halo density [31] (see also [32] for a recent discussion of light fermionic dark matter). Thus, at or below the percent level, neither bound should be imported from an all-dark-matter sterile-neutrino scenario without rescaling.

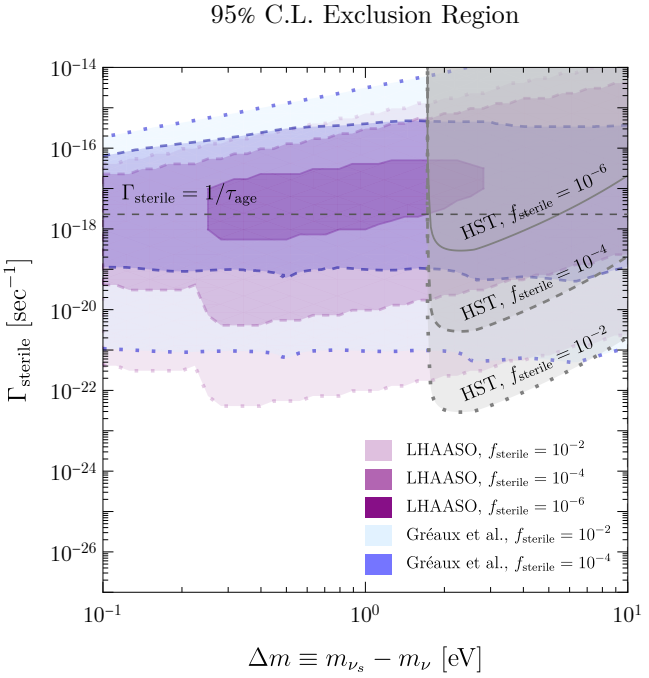


FIG. 3. 95% confidence exclusions for the sterile-neutrino radiative width versus mass splitting. Purple: LHAASO [7]; blue: Gréaux et al. [6]. Only the closed shaded regions are excluded. Fractions in the legend are defined at recombination; $m_\nu = 0.05\,\text{eV}$ is used as a benchmark , and the radiative branching ratio is unity. The gray contours show HST constraints from cosmic optical background anisotropies [33, 34].

Cold parents at recombination are an input to the decay calculation. We remain agnostic to its production mechanism. Pauli exclusion nevertheless sets a minimum momentum spread at fixed abundance. The check in Table I of the Supplemental Material shows that a distribution with $p_F/m_{\nu_s} \leq 0.1$ at recombination is possible only for $\Delta m \gtrsim 1.35, 0.393, 0.090\,\text{eV}$ for the three fractions above, respectively. Smaller splittings require assessing the parent momenta during the emission history.

Unlike a simple upper limit, the exclusions in Fig. 3 form closed regions. At small widths too few photons are produced, whereas at large widths the parent population decays before the epochs to which the EBL measurement is most sensitive. The bound therefore depends on both the initial abundance and its subsequent depletion.

Axion decay

For an axion coupled to electromagnetism through $\mathcal{L} \supset -g_{a\gamma\gamma} a F_{\mu\nu}\widetilde{F}^{\mu\nu}/4$, each decay produces two photons ($N_\gamma = 2$), with

$$E_* = \frac{m_a}{2}, \qquad \Gamma_{a\to\gamma\gamma} = \frac{g_{a\gamma\gamma}^2 m_a^3}{64\pi}. \tag{10}$$

We assume axions constitute all dark matter at recombination. The predicted photon density scales with the initial axion abundance and with $g_{a\gamma\gamma}^2$. In Fig. 4, the solid black and dotted gray lines mark decay rates equal to the inverse recombination time and the inverse age of the Universe, respectively. Following the γ-ray attenuation approach of [11] but with updated data that are consistent across different EBL measurements, we also show a competitive constraint around $m_a \simeq 10\,\mathrm{eV}$.

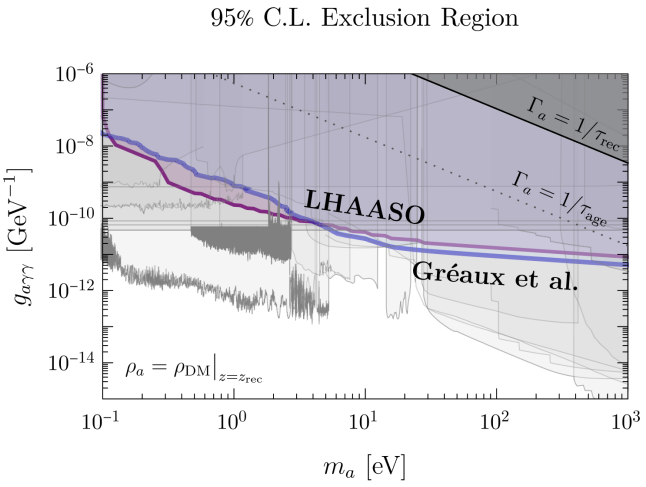


FIG. 4. 95% confidence exclusions for the axion–photon coupling (regions above the boundaries). Purple: LHAASO [7]; blue: Gréaux et al. [6]. Gray: existing constraints [11, 33–65]. The gray comparisons retain their original abundance assumptions and confidence conventions. Axions initially equal the dark-matter abundance at recombination in this work.

CONCLUSION

In this Letter, we demonstrate that TeV transparency, as an independent state-of-the-art measurement EBL in the $10^{-2} - 10$ eV energy range, can be a powerful probe of new physics beyond the standard model. As it provides one of the most stringent measurements of EBL to-date, any new physics that injects photons that fall into this band today can be constrained. We derive strong constraints on the active-neutrino electromagnetic transition moment, the sterile-neutrino radiative decay rate, and the axion-photon coupling. We note that while the intrinsic spectra of TeV gamma-ray sources remain under study, hiding a new-physics EBL contribution would require source-specific exponential hardening for various TeV gamma-ray sources, which is hard. On the other hand, a better measurement of EBL and an improved modeling of the TeV gamma ray sources would most definitely improve the constraint we derive here.

Acknowledgement We thank Yifan Chen, Chao-Qiang Geng, Tao Liu, Andrew Long, Mehrdad Mirbabayi, Giovanni Villadoro, Hyung Do Kim, Hang Bae Kim, and Yue-Liang Wu for useful communications. HS was supported by the Deutsche Forschungsgemeinschaft under Germany Excellence Strategy — EXC 2121 "Quantum Universe" — 390833306. HS appreciates the financial support and warm hospitality of the CERN Theory Group during the visit. CS is partly supported by National Natural Science Foundation of China (NSFC) under Grant No. 12547104. SY is supported by Basic Science Research Program through the National Research Foundation of Korea(NRF) funded by the Ministry of Education(No. RS-2026-25571203) and by IBS under the project code, IBS-R018-D1. HS and CS thank the organizers of the workshop "Axion-Photon Conversion: Terrestrial and Cosmic Searches", during which stimulating discussions and interesting program helped improved this work. HS and SY thank APCTP, Pohang, Korea for their hospitality during the Focus Program [APCTP-2026-F01] from which this work greatly benefited.

Supplemental Material

CONTENTS

I. Optical Depth and EBL Number Density 6

II. Methodology 7
1. The Greaux data set 7
2. LHAASO gamma ray data 7
3. Comparison statistic and construction of contours 7

III. Generic constraints on monochromatic photon injections 7

IV. Assumptions and self-consistency check 9
1. Fermionic phase-space consistency of the sterile benchmarks 9
2. Inhomogeneous EBL contributions 10
3. Dependence on the spectral shape 10
4. Boosted parent particle and its impact 12

V. Decay-induced EBL versus direct axion absorption 13

VI. Comparison of neutrino dipole probes 14

I. OPTICAL DEPTH AND EBL NUMBER DENSITY

We use the energy convention of the main text: $E_{\rm UV}$ is the gamma-ray energy observed *today*, and $E_{\rm IR}$ is the local EBL photon energy *at redshift* z. The density $dn_\gamma/dE_{\rm IR}$ is per unit proper volume and local energy. At $z=0$, $E_{\rm IR}$ is also the energy measured today.

For an isotropic background, a gamma ray crossing a proper distance $d\ell$ accumulates optical depth

$$d\tau_\gamma = d\ell \int_{-1}^{1} d\mu\, \frac{1-\mu}{2} \times \int_{E_{\rm IR}^{\rm th}}^{\infty} dE_{\rm IR}\, \frac{dn_\gamma}{dE_{\rm IR}}(E_{\rm IR},z)\sigma_{\gamma\gamma}(s), \tag{A1}$$

where $\mu = \cos\theta$, $s = 2(1+z)E_{\rm UV}E_{\rm IR}(1-\mu)$, and $E_{\rm IR}^{\rm th} = 2m_e^2/[(1+z)E_{\rm UV}(1-\mu)]$, as in Eq. (2). The factor $1-\mu$ comes from the relativistic collision flux: restoring c, the collision rate contains $c(1-\mu)$, whereas the gamma ray travels $d\ell = c\,dt$. The factor $1/2$ comes from averaging directions in an isotropic background after integrating over the azimuthal angle. The survival probability is $e^{-\tau_\gamma}$.

Along the photon path, a redshift interval corresponds to proper distance

$$d\ell = |dt| = \frac{dz}{(1+z)H(z)}. \tag{A2}$$

Substituting this path length into Eq. (A1) and integrating from $z=0$ to the source redshift z_s gives Eq. (2).

The same photon density determines the spectral intensity νI_ν used in the EBL comparison:

$$[\nu I_\nu](E_{\rm IR},z) = \frac{E_{\rm IR}^2}{4\pi}\frac{dn_\gamma}{dE_{\rm IR}}(E_{\rm IR},z). \tag{A3}$$

The two powers of $E_{\rm IR}$ convert photon number to energy and a linear energy interval to a logarithmic interval. Isotropy supplies the factor $1/(4\pi)$. Restoring ordinary units multiplies the right-hand side by c. The residual EBL data constrain this intensity at $z=0$.

For the decay contribution, we use E_*, N_γ, Γ_X, and the comoving parent density $n_{X,c}$ already defined in the main text. A photon emitted at redshift z_* with energy E_* has local energy $E_{\rm IR}$ at redshift z. At fixed z, its redshift relation gives

$$1+z_* = (1+z)\frac{E_*}{E_{\rm IR}}, \qquad \left|\frac{dt(z_*)}{dE_{\rm IR}}\right| = \frac{1}{E_{\rm IR}H(z_*)}. \tag{A4}$$

Here $t(z_*)$ is cosmic time at emission. The number of photons produced per comoving volume in an emission interval is $N_\gamma\Gamma_X n_{X,c}(z_*)\,dt(z_*)$. Converting emission time to local photon energy with Eq. (A4), and comoving to proper volume with $(1+z)^3$, gives

$$\frac{dn_\gamma}{dE_{\rm IR}}(E_{\rm IR},z) = \frac{(1+z)^3 N_\gamma \Gamma_X n_{X,c}(z_*)}{E_{\rm IR}H(z_*)}\Theta(E_*-E_{\rm IR}). \tag{A5}$$

The step function restricts emission to $z_* \geq z$. The parent density includes depletion and is set to zero outside

the modeled parent history. At $z = 0$, this reduces to Eq. (7); see also Ref. [11]. This is the photon density used in the decay-opacity calculation.

II. METHODOLOGY

We compare the decay signal separately with the present-day residual EBL and the LHAASO gamma-ray spectra. The predictions follow from Eqs. (A3) and (A5), using the parent abundances specified for each particle scenario.

1. The Greaux data set

We use eight residual intensity points at $z = 0$ from the EBL reconstruction of Gréaux et al. [6], in units of $\mathrm{nW\,m^{-2}\,sr^{-1}}$. The residual is the gamma-ray-inferred total EBL minus the integrated galaxy light (IGL) at the corresponding wavelengths. The IGL estimates of Driver et al. [2] and Koushan et al. [66] integrate measured galaxy fluxes and number counts from surveys including GAMA, COSMOS, DEVILS, and Hubble deep fields, with infrared observations from Spitzer and Herschel. They are observational estimates with fitted count distributions and faint-source extrapolations. We use the digitized, already-subtracted residuals and their asymmetric errors.

For each parameter point, we average the predicted decay intensity $[\nu I_\nu]_{\rm NP}(E_{\rm IR}, 0)$ over each energy bin: the intensity is integrated over energy and divided by the bin width. The bins are centered on the digitized energy points and share a logarithmic width equal to their mean logarithmic spacing. We retain the signed residuals, including negative central values, when comparing them with the non-negative decay signal. This comparison uses the reconstructed EBL points without refitting the underlying STeVECat spectra.

2. LHAASO gamma ray data

For GRB 221009A at $z_s = 0.151$, we use the digitized high-energy subset of the LHAASO spectra [7]: six flux points from 230–300 s and seven from 300–900 s after the trigger, spanning approximately 4–12 TeV.

The conventional EBL represents stellar emission and dust reprocessing accumulated over cosmic history. We adopt the Saldana-Lopez et al. [67] template, constructed from HST/CANDELS galaxy photometry using stellar and dust emission templates and completeness corrections, with the LHAASO-fitted rescaling. Its multiplicative factors are 1.30, 1.20, and 0.40 for wavelengths below $8\,\mu$m, between 8 and $28\,\mu$m, and above $28\,\mu$m, respectively [7]. We interpolate the central present-day curve logarithmically in energy and intensity. At redshift z, we evaluate that curve at $E_{\rm IR}/(1+z)$ and multiply the intensity by $(1+z)^4$. The intensity is set to zero when $E_{\rm IR}/(1+z)$ lies outside the tabulated energy range. This approximates the background evolution by photon redshifting and dilution, without additional galaxy emission.

The predicted flux in each observing interval is

$$\Phi_{\rm pred}(E_{\rm UV}) = \Phi_{\rm int}(E_{\rm UV}) e^{-\tau_\gamma^{\rm gal} - \tau_\gamma^{\rm NP}}, \tag{B1}$$

where both optical depths are evaluated at $(E_{\rm UV}, z_s)$ using Eq. (2). We evaluate the digitized intrinsic curves by linear interpolation at the observed energies. These curves and the conventional EBL remain fixed as the decay parameters vary.

3. Comparison statistic and construction of contours

For either comparison, we calculate

$$\chi^2 = \sum_i \frac{(M_i - y_i)^2}{\sigma_i^2}, \tag{B2}$$

where y_i is the measured intensity or flux and M_i its prediction. We use the upper error when $M_i \geq y_i$ and the lower error otherwise, treating the supplied errors as independent. For LHAASO, the statistic is summed over both observing intervals. The two data comparisons produce separate contours and are not combined into a joint statistic.

At each scanned parameter point, we form

$$\Delta\chi_0^2 = \chi^2 - \chi^2_{\rm no\,decay}. \tag{B3}$$

The reference is zero added intensity for the residual EBL and zero added opacity for LHAASO. We display the numerical threshold $\Delta\chi_0^2 = 3.84146$.

The particle-specific scans use logarithmic parameter grids over the ranges shown and retain the imposed lifetime restriction $\Gamma_X[t(1100) - t(10^7)] \leq 1$, where $t(z)$ is cosmic time. Points outside this restriction are masked rather than excluded by the data. The generic scan described below omits this lifetime restriction.

III. GENERIC CONSTRAINTS ON MONOCHROMATIC PHOTON INJECTIONS

The decay calculation can be expressed in terms of three parameters: the photon energy at emission E_*, the total parent decay rate Γ, and the dimensionless photon-weighted abundance

$$\xi \equiv \frac{N_\gamma B_\gamma n_{X,c}(z_{\rm ref})}{1\,\mathrm{cm^{-3}}}, \qquad z_{\rm ref} = 1100. \tag{C1}$$

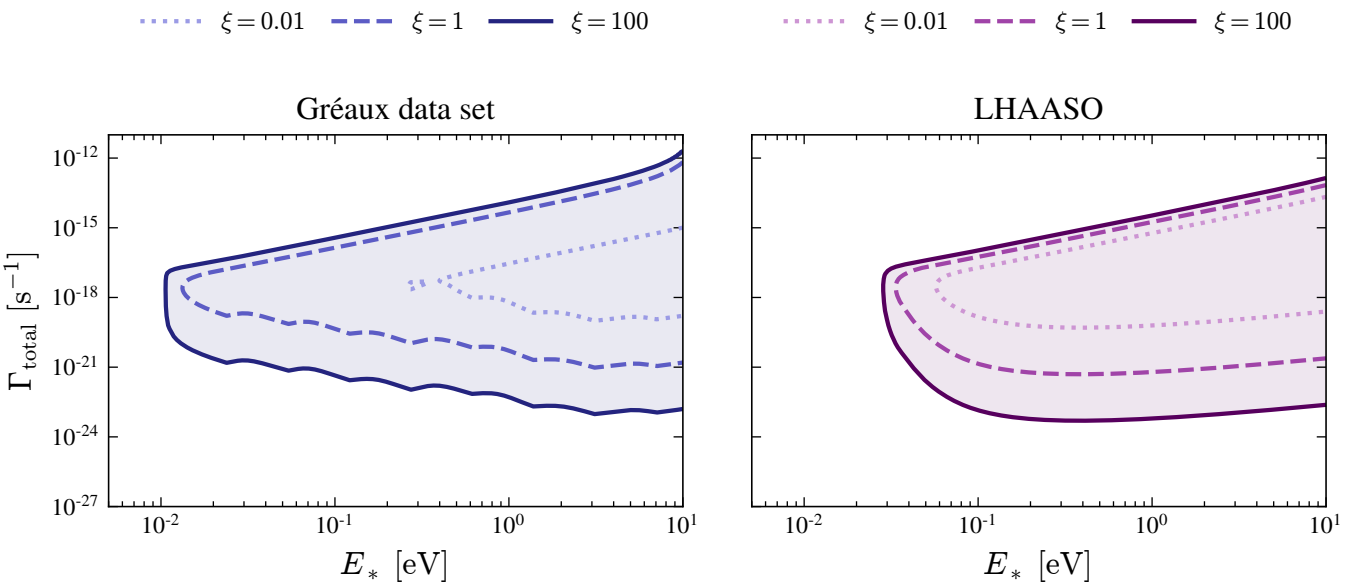


FIG. 5. Generic decay constraints for $\xi = 10^{-2}, 1, 10^{2}$ at $z_{\rm ref} = 1100$ [Eq. (C1)]. Blue (left): residual EBL; purple (right): LHAASO. Dotted, dashed, and solid curves denote increasing ξ, with darker shades for larger values. Curves mark $\Delta\chi^2_0 = 3.84146$; shading shows the region above threshold for $\xi = 10^2$. Background EBL and source spectra are fixed, with no lifetime cut.

Here $n_{X,c}$ is the comoving parent number density, N_γ is the number of photons at energy E_* per radiative decay, and $B_\gamma = \Gamma_{\rm rad}/\Gamma$ is the radiative branching fraction. Thus ξ measures the available photon yield per comoving volume at recombination; it is neither a dark-matter fraction nor the surviving parent abundance today. Photon multiplicity, branching fraction, and reference abundance are degenerate at fixed Γ.

For homogeneous, nonrelativistic parents with a constant decay rate, freely propagating photons, and the fixed background cosmology used here, Eq. (A5) becomes

$$\frac{dn_\gamma}{dE_{\rm IR}}(E_{\rm IR}, z) = \frac{(1+z)^3(1\,{\rm cm}^{-3})\xi\Gamma}{E_{\rm IR}H(z_*)} e^{-\Gamma[t(z_*)-t(z_{\rm ref})]} \times \Theta(z_* - z)\Theta(z_{\rm ref} - z_*), \tag{C2}$$

where $1 + z_* = (1+z)E_*/E_{\rm IR}$. The decay contributions to both observables therefore obey

$$\left([\nu I_\nu]_{\rm NP}, \tau_\gamma^{\rm NP}\right) = \xi\left([\nu I_\nu]_{\rm NP}, \tau_\gamma^{\rm NP}\right)_{\xi=1} \quad \text{at fixed } (E_*, \Gamma). \tag{C3}$$

One set of response tables in (E_*, Γ) consequently suffices for all abundances and particle models satisfying these assumptions. The total rate cannot generally be absorbed into ξ, since it also sets the exponential depletion and hence the spectral shape. Only when $\Gamma[t(z_*) - t(z_{\rm ref})] \ll 1$ throughout the relevant emission history do the predictions depend on E_* and the product $\xi\Gamma$ alone, even if $B_\gamma = 1$.

Figure 5 shows three fixed-ξ slices of this common constraint. For each data set we evaluate

$$\Delta\chi^2_0(E_*, \Gamma, \xi) = \chi^2(E_*, \Gamma, \xi) - \chi^2(\xi = 0). \tag{C4}$$

For the eight present-day residual EBL points, we average the prediction over top-hat energy windows centered on each point. Their common logarithmic width is the mean logarithmic point spacing, and we use the asymmetric errors. The LHAASO comparison uses the 13 high-energy flux points, with the conventional EBL opacity and intrinsic source spectra held fixed. Each normalization is applied to the intensity and additional opacity before computing the statistic; neither χ^2 nor the attenuated flux scales linearly with ξ. We display the nominal threshold $\Delta\chi^2_0 = 3.84146$, without a nuisance-parameter refit or a confidence-level calibration.

Where depletion is negligible, the low-rate boundaries move downward in inverse proportion to ξ. At larger rates, depletion removes parents before the later emission needed to populate the observed bands, producing an upper boundary. The adopted top-hat EBL bins and their unequal residuals and errors give the lower edges their scalloped shape and can produce disconnected islands, as for $\xi = 10^{-2}$ in the left panel.

We specify the reference abundance independently of the parent lifetime. The generic scan imposes no restriction $\Gamma^{-1} > t(z_{\rm ref})$ and does not constrain the mechanism that produces the reference population. A population specified at an earlier epoch z_i is mapped using $n_{X,c}(z_{\rm ref}) = n_{X,c}(z_i)e^{-\Gamma[t(z_{\rm ref})-t(z_i)]}$. For the plotted range $E_* \leq 10\,{\rm eV}$, the supplied EBL bin edges and gamma-ray energies restrict contributing emission to $z_* < 944$ and $z_* < 603$, respectively. Photons emitted before recombination therefore do not contribute in these bands, so this conversion also reproduces the earlier-

normalized active-neutrino calculation within its cold-parent approximation.

For example, axions map through $E_* = m_a/2$ and $\xi = 2f_a\rho_{\rm DM,0}/[m_a(1\,{\rm cm}^{-3})]$, whereas sterile neutrinos with unit radiative branching map through $E_* = (m_{\nu_s}^2 - m_\nu^2)/(2m_{\nu_s})$ and $\xi = f_{\rm sterile}\rho_{\rm DM,0}/[m_{\nu_s}(1\,{\rm cm}^{-3})]$; the fractions here are specified at recombination. One active-neutrino parent eigenstate with unit radiative branching uses $E_* = \Delta m^2/(2m_i)$ and $\xi = 113e^{-\Gamma[t(z_{\rm ref})-t(z_i)]}$ with $z_i = 2\times10^9$. The model-specific plots thus follow by substituting the appropriate normalization and converting coordinates, without repeating the cosmological and pair-production integrals. Any particle decaying into a monochromatic photon line under these assumptions must satisfy this constraint, independently of its spin or decay operator. Relativistic parents, broad spectra, and photon reprocessing require extensions.

IV. ASSUMPTIONS AND SELF-CONSISTENCY CHECK

We examine the consistency of the assumed parent populations and the treatment of the spatial and spectral distributions of the EBL.

1. Fermionic phase-space consistency of the sterile benchmarks

The sterile-neutrino calculation specifies an abundance at $z_{\rm ref} = 1100$ and uses nonrelativistic parents, without deriving their production or thermal history. A necessary consistency check follows from Pauli exclusion, even at zero temperature [68]. Let $F(\boldsymbol{p})$ be the occupation per internal state, with $0 \le F \le 1$, and take $g_s = 2$ available states. At fixed physical number density, the smallest momentum moments occur for the filled Fermi sphere $F = \Theta(p_F - p)$:

$$n_s = \frac{g_s}{(2\pi)^3}\int d^3p\, F(\boldsymbol{p}) = \frac{g_s p_F^3}{6\pi^2}, \qquad p_{\rm rms,min} = \sqrt{\frac{3}{5}}\,p_F. \tag{D1}$$

A population with $p_{\rm rms} \ll m_{\nu_s}$ requires $p_F/m_{\nu_s} \ll 1$; a production spectrum with lower occupation can be warmer than this minimum.

Bar et al. [69] used this minimum-dispersion argument to show that nonthermal production alone cannot evade cosmological free-streaming bounds, revisiting the proposal of Randall et al. [70]. Their structure-formation bound assumes the fermions constitute the dark matter and is not applied directly to our subdominant, decaying populations.

The normalization actually supplied to the decay calculation is

$$n_s(z_{\rm ref}) = \frac{f_{\rm sterile}\rho_{\rm DM,0}}{m_{\nu_s}}(1+z_{\rm ref})^3, \qquad m_{\nu_s} = \Delta m + 0.05\,{\rm eV}. \tag{D2}$$

Here $f_{\rm sterile}$ normalizes the rest-mass density; it equals the energy-density fraction $\rho_s/\rho_{\rm DM}$ only in the nonrelativistic regime. Using $\rho_{\rm DM,0} = 1.264\times10^3\,{\rm eV\,cm^{-3}}$, consistent with $\Omega_{\rm DM}h^2 = 0.120$, gives

$$\eta_F \equiv \frac{p_F(z_{\rm ref})}{m_{\nu_s}} = 0.1566\left(\frac{f_{\rm sterile}}{10^{-2}}\right)^{1/3}\left(\frac{2}{g_s}\right)^{1/3}\left(\frac{1\,{\rm eV}}{m_{\nu_s}}\right)^{4/3} \times \frac{1+z_{\rm ref}}{1101}. \tag{D3}$$

For a chosen ratio η, the condition $\eta_F \le \eta$ therefore requires

$$m_{\nu_s} \ge 0.2489\,{\rm eV}\left(\frac{f_{\rm sterile}}{10^{-2}}\right)^{1/4}\left(\frac{2}{g_s}\right)^{1/4} \times \left(\frac{1+z_{\rm ref}}{1101}\right)^{3/4}\eta^{-3/4}. \tag{D4}$$

The case $\eta = 1$ marks an order-one momentum, not a cold population. We also give $\eta = 0.1$ as an illustrative criterion: in the filled-sphere distribution every particle then has $v < 0.1$, and $p_{\rm rms}/m_{\nu_s} \le 0.0775$.

For example, $\Delta m = 0.1\,{\rm eV}$ corresponds to $m_{\nu_s} = 0.15\,{\rm eV}$ and gives $\eta_F = 1.96, 0.423, 0.0912$ for $f_{\rm sterile} = 10^{-2}, 10^{-4}, 10^{-6}$, respectively. The first benchmark cannot have a deeply nonrelativistic population at recombination even in the minimum-momentum configuration; the smallest fraction allows the chosen $\eta_F \le 0.1$ criterion. The thresholds concern the parent mass, so the daughter mass must be added to the splitting plotted in Fig. 3.

Passing the $\eta = 0.1$ check permits the illustrative cold distribution but does not show that a particular production mechanism creates it. Taking only one available internal state raises the parent-mass thresholds by $2^{1/4}$; a maximum occupation $F_{\rm max} < 1$ raises them by a further $F_{\rm max}^{-1/4}$. If parents free-stream after the reference epoch, their momenta redshift as $p \propto 1+z$. Momentum-independent decay reduces the occupation but does not

$f_{\rm sterile}$	$\Delta m_{\rm min}$ $(\eta = 1)$ [eV]	$\Delta m_{\rm min}$ $(\eta = 0.1)$ [eV]
10^{-2}	0.1989	1.3497
10^{-4}	0.02871	0.3926
10^{-6}	0	0.08997

TABLE I. Minimum splittings allowing the indicated Fermi-momentum ratio at recombination, for $g_s = 2$ and $m_\nu = 0.05\,{\rm eV}$. We use $\Delta m_{\rm min} = \max(0, m_{\nu_s}^{\rm min} - m_\nu)$; the zero entry means that $\eta_F < 1$ for every positive splitting. These are applicability checks of the cold-parent assumption, not additional observational exclusions.

cool the surviving particles. Conversely, a population warm at recombination can become nonrelativistic before the later emissions relevant to the EBL. Assessing such a case requires its momentum-dependent decay spectrum and survival history. However, as we see in the check, we only expect $\mathcal{O}(1)$ correction even at as light as $m_{\nu_s} \sim 0.1\,\mathrm{eV}$, while at $m_{\nu_s} \gtrsim 1\,\mathrm{eV}$ the correction is negligible.

2. Inhomogeneous EBL contributions

The finite propagation time of decay photons makes their instantaneous distribution inhomogeneous. For example, temporarily restoring c, a continuously emitting source with daughter-photon luminosity $\dot{N}_\gamma$ produces

$$n_\gamma(r,t) = \frac{\dot{N}_\gamma(t-r/c)}{4\pi c r^2}\Theta(ct-r). \tag{D5}$$

Nevertheless, spatial averaging over sources of number density n_g gives

$$\overline{n}_\gamma(t) = n_g \int 4\pi r^2\, dr\, n_\gamma(r,t) = n_g \int_0^t dt'\, \dot{N}_\gamma(t'). \tag{D6}$$

Regions of enhanced density are therefore compensated by regions of reduced density. Since the pair-production optical depth is linear in the target photon phase-space density, averaging over random lines of sight gives

$$\langle\tau\rangle = \tau[\overline{n}_\gamma]. \tag{D7}$$

Thus, inhomogeneity does not change the ensemble-mean optical depth.

It does, however, affect the flux-averaged attenuation. Defining

$$\langle F_{\rm obs}\rangle = F_{\rm int}\langle e^{-\tau}\rangle \equiv F_{\rm int} e^{-\tau_{\rm eff}}, \tag{D8}$$

convexity of the function implies

$$\tau_{\rm eff} = -\ln\langle e^{-\tau}\rangle \le \langle\tau\rangle. \tag{D9}$$

For small fluctuations,

$$\tau_{\rm eff} = \langle\tau\rangle - \frac{1}{2}\,\mathrm{Var}(\tau) + \cdots, \tag{D10}$$

so clumpiness weakens the effective attenuation inferred from an ensemble of observed fluxes.

To estimate the largest possible effect, consider an idealized model in which every galaxy is surrounded by a uniform photon sphere of radius R_γ, with no decay photons outside. We normalize the density inside the spheres so that the spatial mean, and hence $\overline{\tau}$, remains fixed. For Poisson-distributed galaxies, the mean number of spheres crossed by a path of length D is

$$\lambda = n_g \pi R_\gamma^2 D. \tag{D11}$$

$R_\gamma/R_{\rm gal}$	λ	$1-\tau_{\rm eff}/\overline{\tau}$ $(\overline{\tau}=1)$	$1-\tau_{\rm eff}/\overline{\tau}$ $(\overline{\tau}=10)$
1	1.9×10^{-3}	99.81%	99.981%
10	0.188	81.74%	98.12%
30	1.70	26.59%	83.47%
100	18.85	2.92%	24.43%

TABLE II. Reduction of the flux-averaged effective optical depth in the uniform photon-sphere model. The spatially averaged optical depth $\langle\tau\rangle = \overline{\tau}$ is unchanged.

Averaging over the chord length through each sphere gives

$$\tau_{\rm eff} = \lambda\left[1 - \frac{1-(1+2x)e^{-2x}}{2x^2}\right], \qquad x = \frac{3\overline{\tau}}{4\lambda}. \tag{D12}$$

In the limit of rare, individually opaque spheres, $\tau_{\rm eff} \simeq \lambda$: most sightlines are transparent, while a small fraction are completely absorbed.

Table II shows this deliberately extreme estimate for a galaxy radius $R_{\rm gal} = 10\,\mathrm{kpc}$, number density $n_g = 10^{-2}\,\mathrm{Mpc}^{-3}$, and gamma-ray path length $D = 600\,\mathrm{Mpc}$. The corresponding mean galaxy separation is $d_g = n_g^{-1/3} = 4.6\,\mathrm{Mpc} \simeq 460 R_{\rm gal}$.

This toy model greatly overestimates the physical inhomogeneity of a freely propagating decay background. A radius of 1 Mpc corresponds to only 3.3 Myr of propagation, whereas decay photons relevant to the cosmological EBL generally accumulate for hundreds of Myr or several Gyr. After 1 Gyr their propagation radius is approximately 300 Mpc; the benchmark path then samples contributions from $\lambda \simeq 1.7\times10^6$ source spheres. Equation (D12) gives a fractional reduction of only 3×10^{-7} for $\overline{\tau}=1$ and 3×10^{-6} for $\overline{\tau}=10$. A substantial correction therefore requires either a photon horizon below a few Mpc, as could occur extremely close to the pair-production threshold, or a rare and transient source population.

Finally, the target field near an individual galaxy is anisotropic. Daughter photons streaming outward from the gamma-ray host are approximately co-propagating with an escaping TeV photon, suppressing both the $(1-\cos\theta)$ collision factor and the pair-production rate. Positive source clustering can instead enhance the conditional optical depth near the host, but only over the galaxy correlation length, which is short compared with a cosmological gamma-ray path. These endpoint and angular corrections are therefore expected to be subleading. The homogeneous EBL calculation should consequently be an excellent approximation for the mean opacity in the parameter region considered here.

3. Dependence on the spectral shape

The attenuation of a gamma ray depends on the spectral distribution of the EBL, rather than only on its bolo-

metric intensity, because pair production selects a finite range of target-photon wavelengths at each gamma-ray energy. It is therefore important that the spectral basis used in the EBL reconstruction can also represent the nonstandard component considered here. Gréaux et al. [6] parametrized the present-day EBL with eight overlapping Gaussian basis functions in logarithmic wavelength,

$$\nu I_\nu(\ell) = \sum_{i=1}^{8} a_i \exp\left[-\frac{(\ell-\ell_i)^2}{2\sigma^2}\right], \qquad \ell = \ln\left(\frac{\lambda}{\lambda_{\rm ref}}\right). \tag{D13}$$

The centers ℓ_i and common width σ are fixed, while the eight amplitudes a_i are fitted independently. For the illustrations below we use $\lambda_i = 0.3\,\mu\mathrm{m}\,e^{(i-1)\Delta\ell}$, with $\Delta\ell = 2\sigma\sqrt{2\ln 2}$, $\sigma/\ln 10 = 0.15$, and $\lambda_{\rm ref} = 0.6\,\mu$m. The eight centers then span 0.3–89.1 μm; the fit covers the quoted response interval 0.18–120 μm. This illustrative grid is offset from the published analytic prescription, which anchors a Gaussian at 0.6 μm. The overlap values below refer to the explicitly specified grid used in both figures. This construction allows the EBL intensity to vary locally in wavelength, although its finite basis width limits the resolution with which a narrow spectral feature can be reconstructed.

We test this explicitly using two physical decay spectra generated from Eq. (A5), including cosmological redshifting and parent depletion. For neutrinos we take normal ordering, $\nu_3 \to \nu_2\gamma$, $E_* = 0.02\,\mathrm{eV}$, and $\mu_{\rm eff} = 10^{-8}\mu_B$. The corresponding masses are $(m_1, m_2, m_3) = (0.03465, 0.03571, 0.06093)\,\mathrm{eV}$, and the radiative width is $\Gamma_\nu = 3.397\times10^{-20}\,\mathrm{s}^{-1}$. We use the standard comoving parent abundance $113\,\mathrm{cm}^{-3}$ at $z_i = 2\times10^9$ and one photon per decay. For axions we take $m_a = 5\,\mathrm{eV}$ and $g_{a\gamma\gamma} = 10^{-10}\,\mathrm{GeV}^{-1}$, giving $E_* = 2.5\,\mathrm{eV}$ and $\Gamma_a = 9.445\times10^{-24}\,\mathrm{s}^{-1}$. Axions initially constitute all dark matter at $z_{\rm ref} = 1100$ and produce two photons per decay. Both spectra are evaluated at $z = 0$ in the nonrelativistic-parent approximation.

For each spectrum $S(\lambda)$, shown in Fig. 6, we use the quoted 0.18–120 μm response range and determine the amplitudes in Eq. (D13) by non-negative least squares, minimizing $\int d\ln\lambda\,[S(\lambda) - B(\lambda)]^2$. The target is set to zero outside its kinematic support. To quantify the agreement we use the symmetric area-overlap coefficient

$$\mathcal{O} = 1 - \frac{\int d\ln\lambda\,|S-B|}{\int d\ln\lambda\,(S+B)} = \frac{2\int d\ln\lambda\,\min(S,B)}{\int d\ln\lambda\,(S+B)}, \tag{D14}$$

where $B(\lambda)$ is the fitted Gaussian sum. Thus $0 \le \mathcal{O} \le 1$, with unity corresponding to identical spectra, including their normalization.

Over the full response interval we find $\mathcal{O}_\nu = 0.748$ and $\mathcal{O}_a = 0.791$. The respective endpoints are $\lambda_* = 61.99\,\mu$m and 0.496 μm. The neutrino fit has one nonzero Gaussian component; the axion spectrum is represented by several components. The broad basis follows the smooth continuum but leaks intensity to wavelengths below the sharp endpoint, reducing the full-interval overlap.

The overlap also depends on the emitted photon energy E_* because the endpoint $\lambda_* = hc/E_*$ moves relative to the fixed Gaussian centers. At fixed decay rate and reference epoch, changing E_* translates the normalized spectrum in logarithmic wavelength,

$$\widehat{S}_{E_*,\Gamma}(\lambda) = \widehat{S}_{E_{*,\rm ref},\Gamma}\left(\lambda\frac{E_*}{E_{*,\rm ref}}\right), \tag{D15}$$

where $\widehat{S}$ denotes intensity divided by its endpoint value, thus factorizing out the overall normalization. We regenerate each spectrum and refit all eight non-negative amplitudes at each E_* over the same response interval. This parametrization applies to all three decay scenarios under the nonrelativistic monochromatic-emission approximation: $E_* = m_a/2$ for axions and $E_* = (m_i^2 - m_f^2)/(2m_i)$ for active or sterile neutrinos. Each curve keeps its decay rate and reference epoch fixed; an overall intensity normalization cancels from $\mathcal{O}$ after the fit.

Changing the lifetime can additionally change the shape through parent depletion. In particular, writing $J = \nu I_\nu$, constant-rate decays give the present-day intensity ratio

$$\frac{J_{\rm dec}(E_{\rm IR},0)}{J_{\rm dec}(E_*,0)} = \frac{E_{\rm IR}}{E_*}\frac{H_0}{H(z_{\rm d})}e^{\Gamma[t_0 - t(z_{\rm d})]}, \tag{D16}$$

where $1+z_{\rm d} = E_*/E_{\rm IR}$, t_0 is the present cosmic age, and the energies lie within the emission history's kinematic support. Larger Γ thus enhances the redshifted tail relative to the endpoint once depletion is important. For $\Gamma t_0 \ll 1$, the exponential is approximately unity: the shape is independent of Γ, which changes only the overall normalization. The overlap generally depends on both E_* and Γ. For the benchmarks above, $\Gamma_\nu t_0 = 0.0148$ and $\Gamma_a t_0 = 4.11\times10^{-6}$, so both are close to the long-lived regime. The energy scan holds the quoted rates fixed; the couplings are specified at the two benchmark energies and are not held fixed along these curves.

Figure 7 shows the dependence on E_* at the two benchmark rates. The overlap varies non-monotonically as the endpoint moves across the fixed basis. Away from the response boundaries, the modulation approximately repeats when E_* changes by the Gaussian spacing factor $e^{\Delta\ell} = 2.26$. Near the long-wavelength boundary, the overlap falls further as the endpoint approaches 120 μm ($E_* = 0.0103\,\mathrm{eV}$). Overall, we observe a good coverage of the chosen basis in Gréaux et al. [6] to represent the monochromatic photon signals we discuss in this work.

This overlap is evaluated at $z = 0$: the fitted decay spectrum already includes cosmological redshifting from its emission history. A photon emitted at redshift $z_{\rm d}$ with energy E_* has local energy $E_{\rm IR} = E_*(1+z)/(1+z_{\rm d})$ at a later epoch $z \le z_{\rm d}$. The Gaussian basis describes

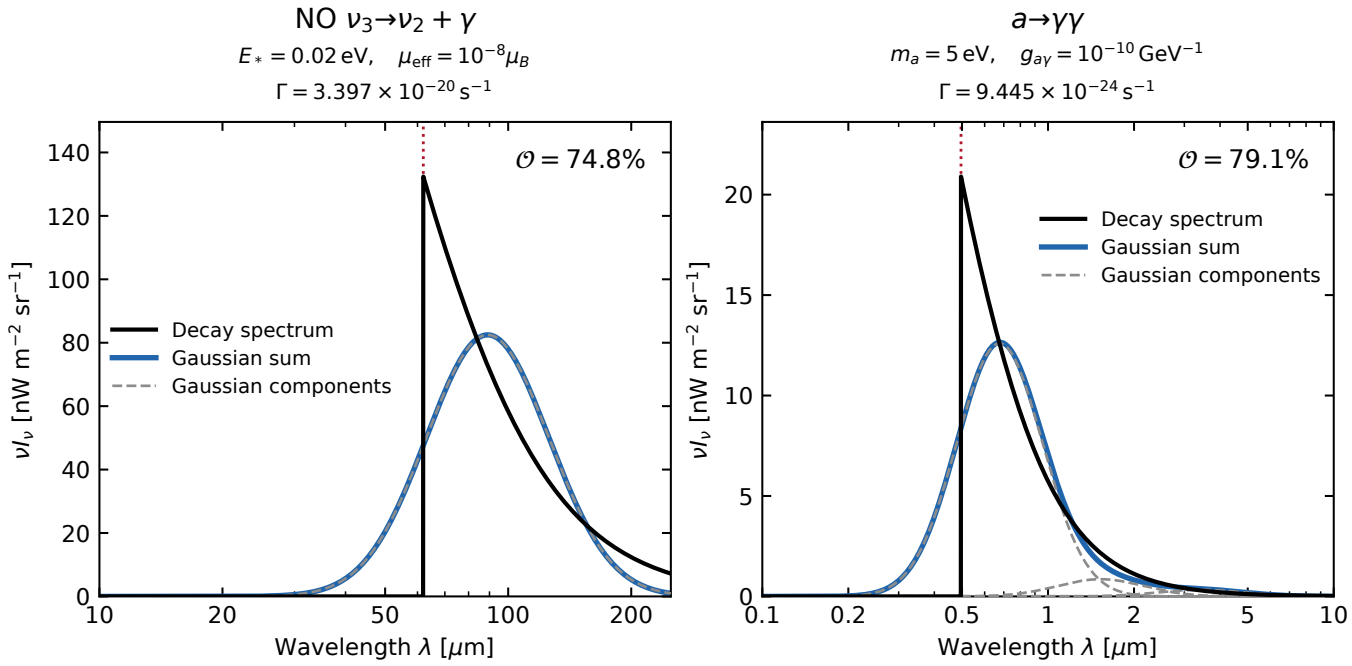


FIG. 6. Non-negative eight-Gaussian fits (blue) to regenerated present-day decay spectra (black). Left: normal-ordering $\nu_3 \to \nu_2\gamma$ with $E_* = 0.02\,\mathrm{eV}$ and $\mu_{\mathrm{eff}} = 10^{-8}\mu_B$, giving $\Gamma_\nu = 3.397 \times 10^{-20}\,\mathrm{s}^{-1}$. Right: $m_a = 5\,\mathrm{eV}$ and $g_{a\gamma\gamma} = 10^{-10}\,\mathrm{GeV}^{-1}$, giving $\Gamma_a = 9.445 \times 10^{-24}\,\mathrm{s}^{-1}$. Dashed gray curves show the nonzero fitted Gaussian components; the neutrino component coincides with its fitted sum. Dotted red lines mark the endpoints. The overlaps in Eq. (D14) use the full 0.18–120 μm response interval, including wavelengths below each endpoint. Both spectra include redshifting and depletion, with abundances and reference epochs specified in the text.

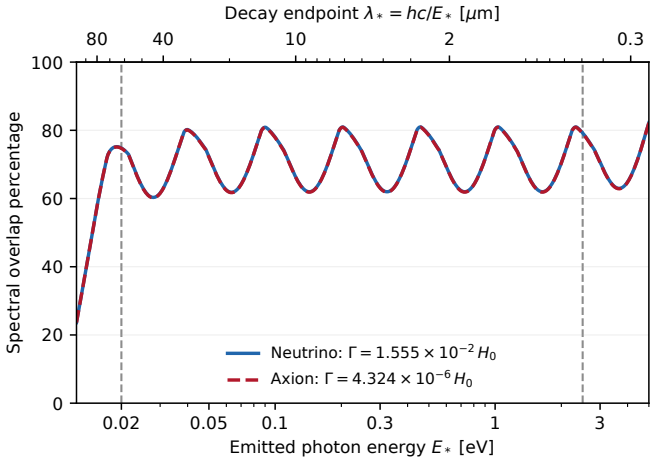


FIG. 7. Present-day spectral overlap as a function of emitted photon energy E_* at the two fixed decay rates used in Fig. 6, expressed in units of $H_0 = 67.4\,\mathrm{km\,s^{-1}\,Mpc^{-1}}$. At each E_* the eight non-negative Gaussian amplitudes are refitted over 0.18–120 μm, including wavelengths below the decay endpoint. Gray dashed vertical lines mark the benchmark energies $E_* = 0.02$ and 2.5 eV; the upper axis gives the endpoint wavelength. The rates, reference epochs, Gaussian centers, and widths remain fixed along each curve.

present-day wavelengths, rather than the photon energy at emission. Gréaux et al. [6] evolve this basis using $J \equiv \nu I_\nu$ and

$$J_{\mathrm{gal}}(E_{\mathrm{IR}}, z) = (1+z)^{4-f_{\mathrm{evol}}} J_{\mathrm{gal}}\left(\frac{E_{\mathrm{IR}}}{1+z}, 0\right), \qquad \text{(D17)}$$

with $1 \le f_{\mathrm{evol}} \le 2$. Its centers in local wavelength are therefore $\lambda_i/(1+z)$, with unchanged logarithmic widths. For continuous decays, fresh photons instead keep the local upper energy endpoint at E_* at every epoch; the local spectrum follows Eq. (A5). The finite Gaussian basis captures a broad decay contribution with energy-dependent accuracy. For the constraints presented here we consequently forward-model the decay photon density at each redshift in the optical depth rather than identifying it with a single combination of the reconstructed EBL amplitudes.

4. Boosted parent particle and its impact

A moving parent lives longer in cosmic time and emits photons over a range of energies even from a two-body decay. Both effects could change the EBL produced by its decay. For relic neutrinos, when the photons probed by the EBL data were emitted matters: a large boost in the early Universe need not imply a large correction

to the EBL measured today. Crudely speaking, the correction stays small as long as the neutrinos become nonrelativistic before the at-rest decay time $1/\Gamma$.

We test this for Fig. 2 by averaging over the standard thermal relic momentum distribution, with isotropic photon emission in the parent rest frame. Thermal momentum effects in radiative neutrino decay are also treated in Ref. [18].

Let q denote the parent momentum redshifted to the present day. The initial number distribution is proportional to $q^2dq/[\exp(q/T_{\nu 0})+1]$, with $T_{\nu 0} = 1.677\times 10^{-4}\,\mathrm{eV}$ and $\langle q\rangle = 3.151T_{\nu 0} = 5.28\times 10^{-4}\,\mathrm{eV}$. At redshift z, its momentum and Lorentz factor are

$$p(q,z) = q(1+z), \qquad \gamma(q,z) = \sqrt{1+\frac{q^2(1+z)^2}{m_i^2}}. \tag{D18}$$

For the normal-ordering $\nu_3 \to \nu_2$ transition used on the top axis of Fig. 2, $m_3 \geq 0.05011\,\mathrm{eV}$. For an undepleted population at this minimum mass, the thermal average gives $\langle\gamma\rangle = 1.000072$ today, 1.000383 at $z = 1.3$, and 11.67 at recombination. The parents therefore pass from relativistic to very slow motion over their history.

Time dilation makes the decay rate per unit cosmic time Γ/γ, where Γ is the rest-frame width. We follow the survival of each momentum separately,

$$S(q,z) = \exp\left[-\Gamma\int_z^{z_i}\frac{dz'}{(1+z')H(z')\gamma(q,z')}\right], \tag{D19}$$

starting at $z_i = 2\times 10^9$ with the same comoving abundance as the cold calculation. For the minimum parent mass, the accumulated proper time to today is, on average, 33.6 Myr shorter than the cosmic elapsed time, about 0.24% of the age of the Universe. Near the upper blue boundary, where depletion is important, this leaves roughly 5% more surviving parents at fixed coupling. The shift of the boundary itself is smaller, as the decay signal there changes steeply with the coupling.

Motion also broadens the photon line. A photon emitted at redshift z_e at rest-frame angle θ_* to the parent's velocity is observed today with energy

$$E_{\gamma 0} = \frac{E_*}{1+z_e}\gamma(q,z_e)\big(1+\beta(q,z_e)\cos\theta_*\big), \tag{D20}$$

where $\beta = p/\sqrt{m_i^2+p^2}$. For isotropic emission, the mean emitted energy is γE_*, while individual photons can be shifted up or down. The early relativistic limit is especially instructive:

$$E_{\gamma 0} \longrightarrow \frac{E_*}{m_i}q(1+\cos\theta_*) \leq q. \tag{D21}$$

The inequality follows from $E_*/m_i \leq 1/2$ for the two-body decay. Cosmological redshift cancels the large early boost, leaving typical photons well below the lowest EBL window, which starts at 0.01059 eV. Reaching that window from the relativistic epoch would require $q/T_{\nu 0} \gtrsim 63$, in the exponentially suppressed tail of the relic distribution.

E_* [eV]	Lower edge [%]	Upper edge [%]
0.012	−0.016	+0.064
0.020	−0.015	+0.242
0.024	+0.196	+0.434

TABLE III. Changes in $\mu_{\rm eff}$ at the lower and upper edges of the residual-EBL exclusion in Fig. 2, including thermal motion and time dilation for normal-ordering $\nu_3 \to \nu_2$. Entries are $100(\mu_{\rm boosted}/\mu_{\rm cold}-1)$; positive values mean that the boundary moves to larger transition moments.

The active-neutrino signal in these EBL windows is consequently produced late. The maximum line energy for the displayed transition is $E_* = 0.02432\,\mathrm{eV}$, so the cold relation $1+z_e = E_*/E_{\gamma 0}$ selects $z_e \lesssim 1.3$. At these epochs the small parent velocities mainly smooth the spectrum, rather than greatly increase its photon energies. We recompute the binned intensity and additional gamma-ray opacity by integrating over the relic momenta and emission angles, retaining the momentum-dependent survival in Eq. (D19). The data, initial abundance, and statistic are held fixed. Table III gives representative changes of the blue boundaries. A finer numerical integration reproduces the shifts at $E_* = 0.024\,\mathrm{eV}$.

For LHAASO, the maximum $\Delta\chi^2_0$ at the active-neutrino endpoint remains 0.784 after including boosts, below the adopted threshold 3.84146. Thus this correction does not generate a purple exclusion within the physical active-neutrino range. The higher-E_* extension of Fig. 2 requires a separate choice of parent mass and momentum distribution. As a thermal example, we take $m_i = 2E_*$, corresponding to a massless daughter and the largest allowed boost for fixed E_* and relic momenta. At $E_* = 0.03\,\mathrm{eV}$, the lower and upper LHAASO boundaries shift by −0.77% and +0.33%; at 0.1 eV the shifts are about −0.001% and +0.10%. These checks concern the stated thermal examples; a hotter or nonthermal population requires specifying its momentum distribution.

V. DECAY-INDUCED EBL VERSUS DIRECT AXION ABSORPTION

One might ask whether the same TeV photons could constrain axions directly, without first converting the axions into an EBL photon population. The axion–photon coupling permits the $2\to 2$ process $\gamma_{\rm UV}a \to \gamma^* \to e^+e^-$. For a nonrelativistic axion its cross section is

$$\sigma_{\gamma a}(s) = \frac{\alpha g_{a\gamma\gamma}^2}{12}\left(1-\frac{m_a^2}{s}\right)\sqrt{1-\frac{4m_e^2}{s}}\left(1+\frac{2m_e^2}{s}\right), \tag{E1}$$

where $s = m_a^2 + 2m_a(1+z)E_{\rm UV}$ at interaction redshift z, above threshold. The corresponding interaction rate per TeV photon is $R_{2\to2} = n_a\sigma_{\gamma a}$.

The process considered in this work is instead axion decay followed by Breit–Wheeler scattering,

$$a \to \gamma_{\rm IR}\gamma_{\rm IR}, \qquad \gamma_{\rm UV}\gamma_{\rm IR} \to e^+e^-. \tag{E2}$$

It may be represented as the $2 \to 3$ reaction $a + \gamma_{\rm UV} \to \gamma_{\rm IR} + e^+e^-$, but its dominant contribution is not an ordinary local three-body process. The internal photon can go on shell: near $q^2 = 0$ the amplitude factorizes as

$$\mathcal{M}_{2\to3} \simeq \mathcal{M}_{a\to\gamma\gamma}\frac{1}{q^2 + i0}\mathcal{M}_{\gamma\gamma\to e^+e^-}. \tag{E3}$$

The on-shell photon can propagate for a cosmological time before interacting. Consequently, the physical regulator of the pole is the finite propagation time and geometry, and the appropriate description is production and transport of real decay photons, as used in Eq. (7).

This makes the two-step channel far more efficient than direct absorption. In the long-lived regime, decay photons accumulate to a density $n_{\gamma,\rm dec} \simeq 2n_a\Gamma_a t$, where $\Gamma_a = g_{a\gamma\gamma}^2 m_a^3/(64\pi)$. The ratio of the instantaneous rates is therefore parametrically

$$\frac{R_{\rm decay+BW}}{R_{2\to2}} \simeq 2\Gamma_a t\,\frac{\overline{\sigma}_{\gamma\gamma}}{\sigma_{\gamma a}} \sim \alpha\frac{m_a^3 t}{m_e^2}. \tag{E4}$$

Although only a small fraction of axions have decayed, each real daughter subsequently interacts through the much larger QED Breit–Wheeler cross section, with no additional axion-coupling suppression. Both rates scale as $n_a g_{a\gamma\gamma}^2$, so their ratio is independent of the axion abundance and of $g_{a\gamma\gamma}$ while depletion is negligible.

For illustration, at $z = 0$, $m_a = 1\,\text{eV}$, and $E_{\rm UV} = 10\,\text{TeV}$, $\Gamma_a t_0 = 3.29 \times 10^{-8} g_{10}^2$, with $g_{10} \equiv g_{a\gamma\gamma}/(10^{-10}\,\text{GeV}^{-1})$, whereas the spectrum-averaged Breit–Wheeler cross section is $9.66 \times 10^{-26}\,\text{cm}^2$, compared with $\sigma_{\gamma a} \simeq 2.37\times10^{-51} g_{10}^2\,\text{cm}^2$. The resulting local rate enhancement is about 2.7×10^{18}; including redshift evolution along the line of sight to GRB 221009A gives an optical-depth ratio of approximately 2.4×10^{18}. Thus the decay-generated EBL probed here overwhelmingly dominates the direct γa channel. The pole contribution and the decay-background opacity are two descriptions of the same physical histories.

VI. COMPARISON OF NEUTRINO DIPOLE PROBES

Different measurements constrain different combinations of neutrino dipole moments. We use the mass-basis matrices μ and ϵ for magnetic and electric moments and define $\lambda = \mu - i\epsilon$. These matrices μ and ϵ are Hermitian; for Majorana neutrinos they are also imaginary and antisymmetric, so only transition moments are allowed. Dirac neutrinos can additionally have diagonal moments [71]. The following scattering expressions assume ultrarelativistic neutrinos and negligible spin conversion during propagation.

Reactor scattering.— Short-baseline reactor experiments such as GEMMA constrain the effective moment of an initially coherent electron-antineutrino state, rather than one mass-basis entry [19, 72]:

$$\mu_R^2 = \sum_j \left|\sum_i U_{ei}(\mu_{ij} + i\epsilon_{ij})\right|^2, \tag{F1}$$

where U is the leptonic mixing matrix and the unobserved final mass eigenstate j is summed incoherently. At finite oscillation distance, U_{ei} acquires the phase $\exp[-im_i^2 L/(2E)]$. Several dipole entries can interfere within each amplitude, making the constraint sensitive to their relative phases.

Solar scattering.— Solar neutrinos reach the detector as an incoherent mixture of mass eigenstates. If $P_{ei}(E)$ is the probability of arriving in state i, the effective scattering moment is

$$\mu_S^2(E) = \sum_i P_{ei}(E)(\lambda^\dagger\lambda)_{ii} = \sum_{ij} P_{ei}(E)|\lambda_{ji}|^2. \tag{F2}$$

The measured recoil spectrum averages this expression over the solar fluxes and detector response [21]. There is no interference between incoming mass eigenstates. In particular, for a single Majorana transition $i \leftrightarrow j$, $\mu_S^2 = (P_{ei} + P_{ej})\mu_{\rm eff}^2$, with $\mu_{\rm eff}$ defined in Eq. (8). Thus solar data also bound individual active transition moments; their limits cannot in general be removed by choosing relative phases [71].

CMB spectral distortions.— Radiative decay and inverse photon absorption distort the CMB spectrum. For a specified transition, COBE/FIRAS constrains the same $\mu_{\rm eff}^2 = |\mu_{ij}|^2 + |\epsilon_{ij}|^2$ that enters the decay width in Eq. (8), with sensitivity set by the masses and relic populations. The calculation of Ref. [18] includes thermal neutrino momenta, stimulated emission, and Pauli blocking, assuming negligible depletion.

This work.— We constrain that same transition strength through its decay-generated photon background: its present-day intensity is compared with the Gréaux residual EBL, and its additional pair-production optical depth is compared separately with LHAASO spectra. Our cold-parent calculation uses the standard relic abundance and a decay-survival factor, with thermal-motion checks in Sec. IV 4. For the physical normal-ordering $\nu_3 \to \nu_2$ range in Fig. 2, the residual-EBL comparison supplies the exclusion band. Complementarity with CMB distortions therefore comes from the photon energies and redshifts probed, rather than a different dipole combination. Several contributing decay channels would require consistent branching fractions

and population evolution. Although scattering and decay probe different effective combinations, this distinction alone does not evade the stronger solar and stellar limits on ordinary active-neutrino transitions.

[1] R. Hill, K. W. Masui, and D. Scott, The Spectrum of the Universe, Applied Spectroscopy **72**, 663 (2018), http://arxiv.org/abs/1802.03694, arXiv:1802.03694 [astro-ph].

[2] S. P. Driver, S. K. Andrews, L. J. Davies, A. S. G. Robotham, A. H. Wright, R. A. Windhorst, S. Cohen, K. Emig, R. A. Jansen, and L. Dunne, Measurements of extragalactic background light from the far UV to the far IR from deep ground- and space-based galaxy counts, Astrophys. J. **827**, 108 (2016), arXiv:1605.01523 [astro-ph.GA].

[3] M. Postman, T. R. Lauer, J. W. Parker, J. R. Spencer, H. A. Weaver, J. M. Shull, S. A. Stern, P. Brandt, S. J. Conard, G. R. Gladstone, C. M. Lisse, S. D. Porter, K. N. Singer, and A. J. Verbiscer, New synoptic observations of the cosmic optical background with New Horizons, Astrophys. J. **972**, 95 (2024), arXiv:2407.06273 [astro-ph.GA].

[4] Q. Yuan, H.-L. Huang, X.-J. Bi, and H.-H. Zhang, Measuring the extragalactic background light from very high energy gamma-ray observations of blazars (2012), arXiv:1212.5866 [astro-ph.HE].

[5] X.-Y. Wang, X.-J. Bi, Z. Cao, P. Vallania, H.-R. Wu, D.-H. Yan, and Q. Yuan, Chapter 3 extra-galactic gamma-ray sources, Chin. Phys. C **46**, 030003 (2022).

[6] L. Gréaux, J. Biteau, and M. Nievas Rosillo, The cosmological optical convergence: Extragalactic background light from TeV gamma rays, Astrophys. J. Lett. **975**, L18 (2024), arXiv:2410.07011 [astro-ph.HE].

[7] Z. Cao *et al.* (LHAASO Collaboration), Very high-energy gamma-ray emission beyond 10 TeV from GRB 221009A, Sci. Adv. **9**, eadj2778 (2023), arXiv:2310.08845 [astro-ph.HE].

[8] A. Baktash, D. Horns, and M. Meyer, Interpretation of multi-TeV photons from GRB221009A, http://arxiv.org/abs/2210.07172 (2022), arXiv:2210.07172 [astro-ph].

[9] J.-G. Guo, H.-J. Li, X.-J. Bi, S.-J. Lin, and P.-F. Yin, Implications of axion-like particles from the Fermi-LAT and H.E.S.S. observations of PG 1553+113 and PKS 2155-304, Chin. Phys. C **45**, 025105 (2021), arXiv:2002.07571 [astro-ph.HE].

[10] L.-Q. Gao, X.-J. Bi, J. Li, R.-M. Yao, and P.-F. Yin, Constraints on axion-like particles from the observation of GRB 221009A by LHAASO, JCAP **2024** (01), 026, arXiv:2310.11391 [astro-ph.HE].

[11] J. L. Bernal, A. Caputo, G. Sato-Polito, J. Mirocha, and M. Kamionkowski, Seeking dark matter with γ-ray attenuation, Physical Review D **107**, 103046 (2023), arXiv:2208.13794 [astro-ph.CO].

[12] Y. Gong, A. Cooray, K. Mitchell-Wynne, X. Chen, M. Zemcov, and J. Smidt, Axion decay and anisotropy of near-IR extragalactic background light, Astrophys. J. **825**, 104 (2016), arXiv:1511.01577 [astro-ph.CO].

[13] X.-J. Bi, A. Addazi, K. Belotsky, V. Beylin, M. Cirelli, A. Esmaili, N. Fornengo, Q.-Y. Gan, M. Kachelriess, M. Khlopov, V. Korchagin, A. Korochkin, V. Kuksa, A. Marciano, A. Neronov, P. Panci, R. Pasechnik, A. Sakharov, F. Sala, G. Di Sciascio, D. Semikoz, P. D. Serpico, N. Volchanskiy, and P.-F. Yin, Chapter 5 dark matter and new physics beyond the standard model with LHAASO, Chin. Phys. C **46**, 030005 (2022).

[14] L. Gréaux, J. Biteau, T. Hassan, O. Hervet, M. Nievas Rosillo, and D. A. Williams, STeVECat, the spectral TeV extragalactic catalog, in *Proceedings of the 7th Heidelberg International Symposium on High-Energy Gamma-Ray Astronomy*, Proceedings of Science, Vol. 417 (2023) p. 171, arXiv:2304.00835 [astro-ph.HE].

[15] R. J. Gould and G. P. Schrëder, Opacity of the universe to high-energy photons, Phys. Rev. **155**, 1408 (1967).

[16] N. Aghanim *et al.* (Planck), Planck 2018 results. VI. Cosmological parameters, Astron. Astrophys. **641**, A6 (2020), [Erratum: Astron.Astrophys. 652, C4 (2021)], arXiv:1807.06209 [astro-ph.CO].

[17] A. Mirizzi, D. Montanino, and P. D. Serpico, Revisiting cosmological bounds on radiative neutrino lifetime, Phys. Rev. D **76**, 053007 (2007), arXiv:0705.4667 [hep-ph].

[18] J. L. Aalberts, S. Ando, W. M. Borg, E. Broeils, J. Broeils, S. Broeils, B. J. Kavanagh, G. Leguijt, M. Reemst, D. R. van Arneman, and H. Vu, Precision constraints on radiative neutrino decay with CMB spectral distortion, Physical Review D **98**, 023001 (2018), http://arxiv.org/abs/1803.00588, arXiv:1803.00588.

[19] A. G. Beda, E. V. Demidova, A. S. Starostin, V. B. Brudanin, V. G. Egorov, D. V. Medvedev, M. V. Shirchenko, and T. Vylov, GEMMA experiment: Three years of the search for the neutrino magnetic moment, Phys. Part. Nucl. Lett. **7**, 406 (2010), arXiv:0906.1926 [hep-ex].

[20] A. G. Beda, V. B. Brudanin, V. G. Egorov, D. V. Medvedev, V. S. Pogosov, M. V. Shirchenko, and A. S. Starostin, The results of search for the neutrino magnetic moment in GEMMA experiment, Adv. High Energy Phys. **2012**, 350150 (2012).

[21] M. Agostini, K. Altenmüller, S. Appel, V. Atroshchenko, Z. Bagdasarian, D. Basilico, G. Bellini, J. Benziger, D. Bick, G. Bonfini, D. Bravo, B. Caccianiga, F. Calaprice, A. Caminata, S. Caprioli, M. Carlini, P. Cavalcante, A. Chepurnov, K. Choi, L. Collica, D. D'Angelo, S. Davini, A. Derbin, X. F. Ding, A. Di Ludovico, L. Di Noto, I. Drachnev, K. Fomenko, A. Formozov, D. Franco, F. Froborg, F. Gabriele, C. Galbiati, C. Ghiano, M. Giammarchi, A. Goretti, M. Gromov, D. Guffanti, C. Hagner, T. Houdy, E. Hungerford, A. Ianni, A. Ianni, A. Jany, D. Jeschke, V. Kobychev, D. Korablev, G. Korga, D. Kryn, M. Laubenstein, E. Litvinovich, F. Lombardi, P. Lombardi, L. Ludhova, G. Lukyanchenko, L. Lukyanchenko, I. Machulin, G. Manuzio, S. Marcocci, J. Martyn, E. Meroni, M. Meyer, L. Miramonti, M. Misiaszek, V. Muratova, B. Neumair, L. Oberauer, B. Opitz, V. Orekhov, F. Ortica, M. Pallavicini, L. Papp, Ö. Penek, N. Pilipenko, A. Pocar, A. Porcelli, G. Ranucci, A. Razeto, A. Re, M. Redchuk, A. Romani, R. Roncin, N. Rossi, S. Schönert, D. Semenov, M. Skorokhvatov, O. Smirnov, A. Sotnikov, L. F. F. Stokes, Y. Suvorov, R. Tartaglia, G. Testera, J. Thurn, M. Toropova, E. Unzhakov, A. Vishneva, R. B. Vogelaar, F. von Feilitzsch, H. Wang, S. Weinz, M. Wojcik, M. Wurm, Z. Yokley, O. Zaimidoroga, S. Zavatarelli, K. Zuber, and G. Zuzel, Limiting neutrino magnetic mo-

ments with Borexino Phase-II solar neutrino data, Physical Review D **96**, 091103 (2017), http://arxiv.org/abs/1707.09355, arXiv:1707.09355 [hep-ex, physics:hep-ph].
[22] C. Giunti and C. A. Ternes, Testing neutrino electromagnetic properties at current and future dark matter experiments, Phys. Rev. D **108**, 095044 (2023), arXiv:2309.17380 [hep-ph].
[23] G. G. Raffelt, Limits on neutrino electromagnetic properties: An update, Phys. Rept. **320**, 319 (1999).
[24] N. Viaux, M. Catelan, P. B. Stetson, G. Raffelt, J. Redondo, A. A. R. Valcarce, and A. Weiss, Particle-physics constraints from the globular cluster M5: Neutrino Dipole Moments, Astronomy & Astrophysics **558**, A12 (2013), http://arxiv.org/abs/1308.4627, arXiv:1308.4627 [astro-ph, physics:hep-ex, physics:hep-ph].
[25] N. Viaux, M. Catelan, P. B. Stetson, G. Raffelt, J. Redondo, A. A. R. Valcarce, and A. Weiss, Neutrino and axion bounds from the globular cluster M5 (NGC 5904), Phys. Rev. Lett. **111**, 231301 (2013), arXiv:1311.1669 [astro-ph.SR].
[26] F. Capozzi and G. Raffelt, Axion and neutrino bounds improved with new calibrations of the tip of the red-giant branch using geometric distance determinations, Phys. Rev. D **102**, 083007 (2020), arXiv:2007.03694 [astro-ph.SR].
[27] C. Giunti, K. Kouzakov, Y.-F. Li, and A. Studenikin, Neutrino Electromagnetic Properties, Ann. Rev. Nucl. Part. Sci. **75**, 1 (2025), arXiv:2411.03122 [hep-ph].
[28] J. L. Bernal, A. Caputo, F. Villaescusa-Navarro, and M. Kamionkowski, Searching for the Radiative Decay of the Cosmic Neutrino Background with Line-Intensity Mapping, Phys. Rev. Lett. **127**, 131102 (2021), arXiv:2103.12099 [hep-ph].
[29] C. A. Ternes and M. Tórtola, Neutrino magnetic moments: effective versus fundamental parameters, Nucl. Phys. B **1019**, 117107 (2025), arXiv:2505.02633 [hep-ph].
[30] A. Boyarsky, J. Lesgourgues, O. Ruchayskiy, and M. Viel, Lyman-α constraints on warm and on warm-plus-cold dark matter models, JCAP **05** (05), 012, arXiv:0812.0010 [astro-ph].
[31] S. Tremaine and J. E. Gunn, Dynamical role of light neutral leptons in cosmology, Phys. Rev. Lett. **42**, 407 (1979).
[32] J. M. Cline, G. Herrera, and J.-S. Roux, Neutrinos as Dark Matter (2026), arXiv:2603.28859 [hep-ph].
[33] K. Nakayama and W. Yin, Anisotropic cosmic optical background bound for decaying dark matter in light of the LORRI anomaly, Phys. Rev. D **106**, 103505 (2022), arXiv:2205.01079 [hep-ph].
[34] P. Carenza, G. Lucente, and E. Vitagliano, Probing the blue axion with cosmic optical background anisotropies, Phys. Rev. D **107**, 083032 (2023), arXiv:2301.06560 [hep-ph].
[35] R. Janish and E. Pinetti, Hunting Dark Matter Lines in the Infrared Background with the James Webb Space Telescope, Phys. Rev. Lett. **134**, 071002 (2025), arXiv:2310.15395 [hep-ph].
[36] E. Pinetti, First constraints on QCD axion dark matter using James Webb Space Telescope observations (2025), arXiv:2503.11753 [hep-ph].
[37] A. K. Saha, S. Bouri, A. Das, A. Dubey, and R. Laha, Shedding infrared light on QCD axion and axionlike particle dark matter with JWST, Phys. Rev. D 10.1103/ks1j-hxk2 (2026), accepted 28 August 2026, arXiv:2503.14582 [hep-ph].
[38] E. Todarello, M. Regis, J. Reynoso-Cordova, M. Taoso, D. Vaz, J. Brinchmann, M. Steinmetz, and S. L. Zoutendijk, Robust bounds on ALP dark matter from dwarf spheroidal galaxies in the optical MUSE-Faint survey, JCAP **2024** (05), 043, arXiv:2307.07403 [astro-ph.CO].
[39] E. Todarello and M. Regis, Bounds on axions-like particles shining in the ultra-violet, JCAP **2025** (05), 070, arXiv:2412.02543 [hep-ph].
[40] W. Yin, T. Bessho, Y. Ikeda, H. Kobayashi, D. Taniguchi, H. Sameshima, N. Matsunaga, S. Otsubo, Y. Sarugaku, T. Takeuchi, H. Kato, S. Hamano, and H. Kawakita, First Result for Dark Matter Search by WINERED, Phys. Rev. Lett. **134**, 051004 (2025), arXiv:2402.07976 [astro-ph.CO].
[41] D. Grin, G. Covone, J.-P. Kneib, M. Kamionkowski, A. Blain, and E. Jullo, A Telescope Search for Decaying Relic Axions, Phys. Rev. D **75**, 105018 (2007), arXiv:astro-ph/0611502.
[42] H. Wang, D. J. Eisenstein, J. N. Aguilar, S. Ahlen, S. Bailey, D. Brooks, T. Claybaugh, A. de la Macorra, P. Doel, J. E. Forero-Romero, A. Kremin, M. E. Levi, M. Manera, R. Miquel, C. Poppett, M. Rezaie, G. Rossi, E. Sanchez, M. Schubnell, G. Tarlé, B. A. Weaver, and Z. Zhou, Spectroscopic search for optical emission lines from dark matter decay, Phys. Rev. D **110**, 103007 (2024), arXiv:2311.05476 [astro-ph.CO].
[43] D. Cadamuro and J. Redondo, Cosmological bounds on pseudo Nambu-Goldstone bosons, JCAP **2012** (02), 032, arXiv:1110.2895 [hep-ph].
[44] P. Arias, D. Cadamuro, M. Goodsell, J. Jaeckel, J. Redondo, and A. Ringwald, WISPy cold dark matter, JCAP **2012** (06), 013, arXiv:1201.5902 [hep-ph].
[45] B. Bolliet, J. Chluba, and R. Battye, Spectral distortion constraints on photon injection from low-mass decaying particles, Mon. Not. Roy. Astron. Soc. **507**, 3148 (2021), arXiv:2012.07292 [astro-ph.CO].
[46] H. Liu, W. Qin, G. W. Ridgway, and T. R. Slatyer, Exotic energy injection in the early universe. II. CMB spectral distortions and constraints on light dark matter, Phys. Rev. D **108**, 043531 (2023), arXiv:2303.07370 [astro-ph.CO].
[47] S. Porras-Bedmar, M. Meyer, and D. Horns, Novel bounds on decaying axionlike particle dark matter from the cosmic background, Phys. Rev. D **110**, 103501 (2024), arXiv:2407.10618 [astro-ph.CO].
[48] K. Langhoff, N. J. Outmezguine, and N. L. Rodd, Irreducible axion background, Phys. Rev. Lett. **129**, 241101 (2022), arXiv:2209.06216 [hep-ph].
[49] A. Ayala, I. Domínguez, M. Giannotti, A. Mirizzi, and O. Straniero, Revisiting the bound on axion-photon coupling from Globular Clusters, Phys. Rev. Lett. **113**, 191302 (2014), arXiv:1406.6053 [astro-ph.SR].
[50] M. J. Dolan, F. J. Hiskens, and R. R. Volkas, Advancing globular cluster constraints on the axion-photon coupling, JCAP **2022** (10), 096, arXiv:2207.03102 [hep-ph].
[51] P. Gondolo and G. G. Raffelt, Solar neutrino limit on axions and keV-mass bosons, Phys. Rev. D **79**, 107301 (2009), arXiv:0807.2926 [astro-ph].
[52] N. H. Nguyen, E. H. Tanin, and M. Kamionkowski, Spectra of axions emitted from main sequence stars, JCAP **2023** (11), 091, arXiv:2307.11216 [hep-ph].

[53] A. Caputo, G. Raffelt, and E. Vitagliano, Muonic boson limits: Supernova redux, Phys. Rev. D **105**, 035022 (2022), arXiv:2109.03244 [hep-ph].

[54] A. Caputo, H.-T. Janka, G. Raffelt, and E. Vitagliano, Low-Energy Supernovae Severely Constrain Radiative Particle Decays, Phys. Rev. Lett. **128**, 221103 (2022), arXiv:2201.09890 [astro-ph.HE].

[55] D. Wadekar and Z. Wang, Strong constraints on decay and annihilation of dark matter from heating of gas-rich dwarf galaxies, Phys. Rev. D **106**, 075007 (2022), arXiv:2111.08025 [hep-ph].

[56] S. Andriamonje *et al.* (CAST), An Improved limit on the axion-photon coupling from the CAST experiment, JCAP **2007** (04), 010, arXiv:hep-ex/0702006.

[57] E. Arik *et al.* (CAST), Probing eV-scale axions with CAST, JCAP **2009** (02), 008, arXiv:0810.4482 [hep-ex].

[58] S. Aune *et al.* (CAST), CAST search for sub-eV mass solar axions with 3He buffer gas, Phys. Rev. Lett. **107**, 261302 (2011), arXiv:1106.3919 [hep-ex].

[59] M. Arik *et al.* (CAST), Search for Solar Axions by the CERN Axion Solar Telescope with ^{3}He Buffer Gas: Closing the Hot Dark Matter Gap, Phys. Rev. Lett. **112**, 091302 (2014), arXiv:1307.1985 [hep-ex].

[60] M. Arik *et al.* (CAST), New solar axion search using the CERN Axion Solar Telescope with ^{4}He filling, Phys. Rev. D **92**, 021101 (2015), arXiv:1503.00610 [hep-ex].

[61] S. Moriyama, M. Minowa, T. Namba, Y. Inoue, Y. Takasu, and A. Yamamoto, Direct search for solar axions by using strong magnetic field and x-ray detectors, Phys. Lett. B **434**, 147 (1998), arXiv:hep-ex/9805026.

[62] Y. Inoue, T. Namba, S. Moriyama, M. Minowa, Y. Takasu, T. Horiuchi, and A. Yamamoto, Search for sub-electronvolt solar axions using coherent conversion of axions into photons in magnetic field and gas helium, Phys. Lett. B **536**, 18 (2002), arXiv:astro-ph/0204388.

[63] Y. Kirita *et al.* (SAPPHIRES), Search for sub-eV axion-like particles in a stimulated resonant photon-photon collider with two laser beams based on a novel method to discriminate pressure-independent components, JHEP **2022** (10), 176, arXiv:2208.09880 [hep-ex].

[64] Y. Kirita *et al.* (SAPPHIRES), Search for sub-eV axion-like particles in a quasi-parallel stimulated resonant photon-photon collider with "coronagraphy", JHEP **2025** (06), 138, arXiv:2409.01805 [hep-ex].

[65] C. O'Hare, AxionLimits (2020).

[66] S. Koushan, S. P. Driver, S. Bellstedt, *et al.*, GAMA/DEVILS: Constraining the cosmic star-formation history from improved measurements of the 0.3–2.2 micron extragalactic background light, Mon. Not. Roy. Astron. Soc. **503**, 2033 (2021), arXiv:2102.12323 [astro-ph.CO].

[67] A. Saldana-Lopez, A. Domínguez, P. G. Pérez-González, J. Finke, M. Ajello, J. R. Primack, V. S. Paliya, and A. Desai, An observational determination of the evolving extragalactic background light from the multiwavelength HST/CANDELS survey in the Fermi and CTA era, Mon. Not. Roy. Astron. Soc. **507**, 5144 (2021), arXiv:2012.03035 [astro-ph.CO].

[68] M. Carena, N. M. Coyle, Y.-Y. Li, S. D. McDermott, and Y. Tsai, Cosmologically Degenerate Fermions (2021), arXiv:2108.02785 [hep-ph].

[69] N. Bar, D. Blas, K. Blum, and H. Kim, Assessing the Fornax globular cluster timing problem in different models of dark matter, Phys. Rev. D **104**, 043021 (2021), arXiv:2102.11522 [astro-ph.GA].

[70] L. Randall, J. Scholtz, and J. Unwin, Cores in dwarf galaxies from Fermi repulsion, Mon. Not. Roy. Astron. Soc. **467**, 1515 (2017), arXiv:1611.04590 [astro-ph.GA].

[71] B. C. Cañas, O. G. Miranda, A. Parada, M. Tórtola, and J. W. F. Valle, Updating neutrino magnetic moment constraints, Physics Letters B **753**, 191 (2016), arXiv:1510.01684 [hep-ph].

[72] W. Grimus and P. Stockinger, Effects of neutrino oscillations and neutrino magnetic moments on elastic neutrino–electron scattering, Physical Review D **57**, 1762 (1998), arXiv:hep-ph/9708279 [hep-ph].